

## The relation between structural, optical, and electronic properties of composite CuO/ZnO in supporting photocatalytic performance

Roni Rahmat<sup>a</sup>, Heryanto Heryanto<sup>a</sup>, Sultan Ilyas<sup>a</sup>, Ahmad Nurul Fahri<sup>a</sup>,  
Inayatul Mutmainna<sup>a</sup>, Mufti Hatur Rahmi<sup>b</sup>, Dahlang Tahir<sup>a,\*</sup>

<sup>a</sup>Department of Physics, Hasanuddin University, Makassar, 90245 – Indonesia, emails: dtahir@fmipa.unhas.ac.id (D. Tahir), ronirahmat02okto@gmail.com (R. Rahmat), heryanto@science.unhas.ac.id (H. Heryanto), sultanilyas13@gmail.com (S. Ilyas), ahmadfahri32474@gmail.com (A.N. Fahri), inayatul.mutmainna@yahoo.co.id (I. Mutmainna)

<sup>b</sup>Fisheries Science Study Program, Hasanuddin University, Makassar, 90245 – Indonesia, email: muftihatur93@gmail.com

Received 24 November 2021; Accepted 1 August 2022

### ABSTRACT

Phase transformation, structural and optical properties of ZnO/CuO composite for various milling times were studied by means of X-ray diffraction (XRD), and Fourier-transform infrared (FTIR) spectroscopy, respectively. The refractive index ( $n$ ), extinction coefficient ( $k$ ), dielectric function, energy-loss function ( $\text{Im}(-1/\epsilon)$ ), and optical absorption coefficient were determined from the quantitative analysis of FTIR spectra by applying Kramers–Kronig relation. Density of states (DOS) was analyzed using Quantum ESPRESSO package. For milling time up to 12 h, crystalline phase is dominant and for >12 h, phase transformation changed from crystalline to amorphous. The crystallite size shows a decrease with increasing the milling time due to Zn and Cu atoms spreading each other and producing the individual crystalline structure. For 20 h milling time, it shows the minimum distance ( $\Delta$ ) between two optical phonon modes due to the enlarging lattice. For various milling time, the density of states (DOS) is similar for each composite due to the crystalline phase (%) for composites also similar. The best degradation percentage is 96.8% and only 30 min irradiation time for sample 1 h milling. For milling 20 h up to 52 h, the degradation decreases from 93.10% to 78.5% and up again to 91.5% for 56 h milling which the trend is opposite with longitudinal optical phonon mode. This study shows powerful method for determining optical properties from FTIR spectra and effective way to investigate the transformation phase and structural properties from XRD spectra of CuO/ZnO composite.

*Keywords:* Milling time; Transformation phase; Structural properties; Optical properties; CuO/ZnO

### 1. Introduction

The textile industry is one of the main sources in increasing water pollution for disposal without prior treatment [1]. In the past few years, some of the small textile industry grew up which had negative effect to the environment in the form of synthetic or organic dyes during the production process for disposal at high toxicity. It is affecting not only the water ecosystem but also human

health [2]. Therefore, treatment of the textile waste using new material before disposal to the environment is urgent solution for providing clean water and green ecosystem.

Photocatalysis is one of the methods that can be the solution for the environment because it can directly involve solar energy to remove numerous pollutants. However, the application of photocatalyst in the environment has not fulfilled the expected consequences because of low photocatalytic performance and high cost on a large scale.

\* Corresponding author.

Pollutants also influence the difficulty of photocatalyst application in the natural environment, water, air, and solid phase, which are diverse and complex [3]. Therefore, we need to handle this situation with increasing material performance of photocatalyst.

Nekouei et al. [4], Loudjani et al. [5] and Ghasedi et al. [6] reported that the materials performance in the macro-scale is greatly influenced by the structural and optical properties in the micro-scale, and these properties strongly depend on the composition and synthesis process. The structural properties such as transformation phase are fundamental knowledge, which is essential to understand correlation between the synthesis and the performance of material [5]. The synthesis methods have been reported by many researchers such as; sol-gel, hydrothermal processing, vapor phase transport, chemical phase transport, and mechanical alloying (MA) [7–11]. One of the synthesis methods using high technology at low temperature by solid-state reaction for powder material is mechanical alloying (MA) [12], which is possible to get a metastable phase [13]. MA which consists of ball collision with the sample's particles is capable of a large number of metastable phases producing such as nanocrystals, supersaturated solid solutions, and amorphous phase [14–16].

MA is used for reducing particle size Titorenkova et al. [17], mixing two or more different types of materials to form alloy or composite [18–21]. There are many researchers reporting the effect of milling time to the structural and optical properties of materials such as; NiTeGe [22], Ti-Mg [23], AlCuNiFeCr [24], Ni-Nb-Y [25], Al-CuO [26], polystyrene/CuO-Fe<sub>2</sub>O<sub>3</sub> [27], and Fe-ZnO [28]. ZnO also is important materials due to high chemical stability, non-toxic, large band gap energy (3.37 eV), high excitation binding energy (~60 meV) [29], and it can be tuned the size and morphology (nanorods, nanosheet, nanoflower, and nanowire) [30–33]. The applications of ZnO have been reported for sensors, solar cells, and optoelectronic devices [34–36]. Singh et al. [29] reported ZnO nanoparticles synthesized using ball milling had an effect on the phase transformation, the crystallite size, and the optical properties.

For CuO, the characteristics are environment-friendly, low cost, and large specific surface area. CuO is a *p*-type semiconductor with the band gap energy of 1.22 eV. There are many applications of CuO such as catalysis [37], battery [38], and gas sensor [39,40]. In this study, the combination between CuO and ZnO in the form of composite CuO/ZnO is synthesized for study the structural and optical properties as essential properties which high correlation in supporting the performance of the material. As long as our knowledge, there is no reported phase transformation and structural properties from the analysis of X-ray diffraction (XRD) spectra, and optical properties from the quantitative analysis of Fourier-transform infrared (FTIR) spectra as a function of milling time for composite CuO/ZnO. We apply mechanical alloying with various milling time up to 56 h and focusing for analysing the structural properties and phase transformation from the XRD spectra, and the optical properties by applying Kramers–Kronig relation from the FTIR spectroscopy spectra. The optical properties will perform in the form of the refractive index (*n*) and extinction coefficient (*k*). From the optical properties,

the longitudinal and transversal optical phonon mode, the complex dielectric function (real part ( $\epsilon_1$ ) and imaginary part ( $\epsilon_2$ )), energy-loss function ( $\text{Im}(-1/\epsilon)$ ), and the optical absorption coefficient are determined. The electronic properties in the form of density of states (DOS) was determined using quantum espresso package. The photocatalytic performance of the textile industrial wastewater is analyzed using UV-Vis spectrometer spectra. The correlation between these properties is also discussed.

## 2. Material and experiment

Zinc oxide (ZnO) and copper(II) oxide powder (CuO) supplied from Merck with particle size is <10  $\mu\text{m}$  and assay 98%. The weight ratio of CuO:ZnO is 1:1 maintained during milling by using MM 400 Retch Mixer Mill at the frequency 10 Hz for 30 min, 1, 2, 6, 4, 8, 12, 16, 20, 24, 28, 28, 32, 36, 40, 44, 44, 48, 52 and 56 h.

Sample characterizations were carried out by using XRD spectroscopy spectra (Shimadzu 7000) with CuK $\alpha$  radiation ( $\lambda = 1.5405 \text{ \AA}$ )  $2\theta$  ranging from 25° to 80°, operation at 30 kV and 10 mA for study the structural properties and phase transformation of CuO/ZnO composites. The optical properties are determined from the quantitative analysis of FTIR spectroscopy spectra by applying the Kramers–Kronig relation, as described in Suryani et al. [41]. The photocatalytic activity is analyzed by using methylene blue (MB) as a model pollutant with an initial concentration is 15% and pH 6 for MB solution, irradiated under a halogen lamp (300 W, OSRAM 645, Germany) which is the distance of 30 cm from MB solution. The experiment was carried out in 100 mL beaker with 0.1 g of composite CuO/ZnO. The MB solution without radiation was ( $C_0$ ) which was the initial concentration. Then 5 mL solution was taken out every 15 min from the reaction for measuring the absorbance assigned ( $C_t$ ). The solutions would be analyzed by using UV-Vis spectroscopy (Shimadzu UV-Vis Spectrophotometer UV-1800).

## 3. Result and discussion

### 3.1. X-ray diffraction

The milling times milling affected the CuO/ZnO crystal system, which means the processing by solid-state reaction influencing the structural properties. The time of milling process increases is not always reducing the particle size. It is strongly depended on the type of materials, but the consistency for lattice phase shift randomly at the beginning of the alloying process [42]. There are two-phase stages in the composites CuO/ZnO; crystalline and amorphous as shown in Fig. 1.

Fig. 1a shows the XRD spectra as a function of milling time from 30 min to 56 h. From the diffraction spectra, *d*-spacing, crystallite size, dislocation density, and strain were determined Feijoo et al. [43]. The XRD spectra in Fig. 1a were divided into two groups; Fig. 1b for crystalline phase dominant and Fig. 1c for amorphous phase dominant.

Fig. 1b shows the XRD spectra for the milling time process from 30 min up to 12 h. It shows the high intensity and sharp compared with the milling times >12 h. For >12 h of milling time the amorphous phase is dominant, which can be

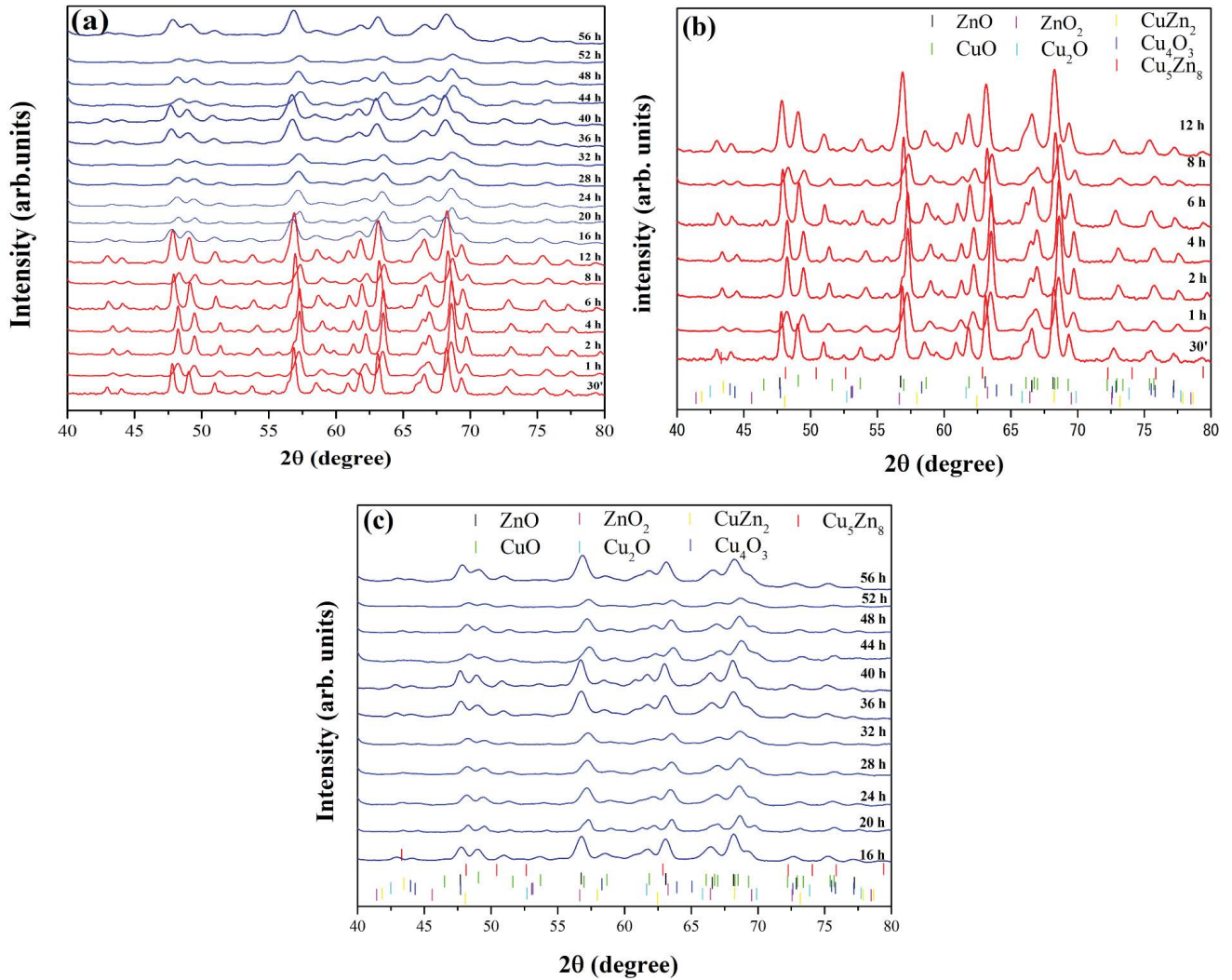


Fig. 1. (a) X-ray diffraction (XRD) spectra of composite CuO/ZnO for various milling times. (b) For 30 min to 12 h and (c) for 16 to 56 h. We have included the existing phase in composite CuO/ZnO for comparison based on JCPDS: CuO (01-074-1021), ZnO (01-079-0205), Cu<sub>4</sub>O<sub>3</sub> (00-049-1830), Cu<sub>2</sub>O (01-074-1230), ZnO<sub>2</sub> (00-013-0311), Cu<sub>5</sub>Zn<sub>8</sub> (00-025-1228), and CuZn<sub>2</sub> (00-039-0400).

identified by the intensity of diffraction peaks low and broad indicated that the full width at half maximum (FWHM) increasing, as can be seen in Fig. 1c. The intensity decreases due to the uniform bonding decrease, which means the broken bond between the atoms increasing Taghvaei et al. [44]. Fig. 1 also shows that the XRD spectra as a function of milling times formed new phase. Based on JCPDS data the phases are CuO (01-074-1021), ZnO (01-079-0205), Cu<sub>4</sub>O<sub>3</sub> (00-049-1830), Cu<sub>2</sub>O (01-074-1230), ZnO<sub>2</sub> (00-013-0311), Cu<sub>5</sub>Zn<sub>8</sub> (00-025-1228) and CuZn<sub>2</sub> (00-039-0400) are identified.

The intensity, full width at half maximum ( $\beta_{hkl}$ ), wavelength of radiation sources ( $\lambda$ ), and diffraction peaks angle ( $\theta$ ) are used in the quantitative analysis for determining the structural properties as described by the study of Ilyas et al. [45]. The value of  $\beta_{hkl}$  is used to determine the crystallite size by Scherrer equation as follows:

$$D = \frac{k\lambda}{\beta_{hkl} \cos\theta} \quad (1)$$

Dislocation density is determined from the crystallite size ( $D$ ) reported by the study of Zak et al. [46]. The parameters of microstrain ( $\epsilon$ ) also contributed to the broadening ( $\beta_{strain}$ ), which are the Scherrer equation becomes:

$$\beta = \beta_{hkl} + \beta_{strain} = \frac{k\lambda}{D \cos\theta} + 4\epsilon \tan\theta \quad (2)$$

where  $\beta$  is full width at half maximum (radian),  $D$  is the crystallite size (nm),  $\epsilon$  is microstrain and  $k$  is Scherrer constant.

Table 1 and Fig. 2 show the relation between the amount of crystalline phase,  $d$ -spacing, dislocation density ( $\delta$ ), strain ( $\epsilon$ ), the crystallite size ( $D$ ) for various milling time (30 min, 1, 20, 40, 44, 52 and 56 h) of CuO/ZnO composite. By this method, there are three relations: (1) relation between crystalline phase, the crystallite size ( $D$ ) and dislocation density ( $\delta$ ), (2) relation between the dislocation density ( $\delta$ ) and the strain ( $\epsilon$ ), and (3) relation between  $d$ -spacing and

Table 1

Relation between *d*-spacing, crystalline size (*D*), dislocation density ( $\delta$ ), strain ( $\epsilon$ ) and crystalline phase from the quantitative analysis of XRD spectra in Fig. 1 for several milling time

| Milling time (h) | <i>d</i> -spacing (Å) | Crystallite size ( <i>D</i> ) (nm) | Dislocation density ( $\delta$ ) ( $\text{nm}^{-2} \times 10^{-3}$ ) | Strain ( $\epsilon$ ) ( $10^{-3}$ ) | Crystalline phase (CP) (%) |
|------------------|-----------------------|------------------------------------|--|-------------------------------------|----------------------------|
| 0.5              | 1.9                   | 26.74                              | 1.39   | 2.72                                | 43.4                       |
| 1                | 1.8                   | 17.05                              | 3.95   | 5.07                                | 55.8                       |
| 20               | 1.81                  | 18.91                              | 3.71   | 4.82                                | 44.5                       |
| 40               | 1.9                   | 13.94                              | 6.28   | 6.53                                | 45.38                      |
| 44               | 1.9                   | 13.94                              | 6.28   | 1.56                                | 46.53                      |
| 52               | 1.88                  | 12.07                              | 9.05   | 1.87                                | 47.98                      |
| 56               | 1.98                  | 10.78                              | 11.42  | 9.03                                | 47.58                      |

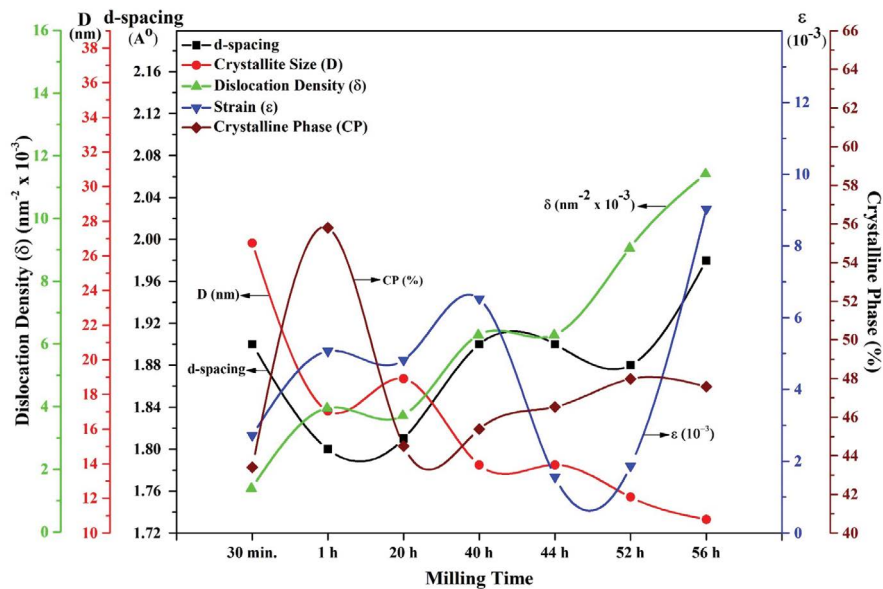


Fig. 2. Relation between *d*-spacing, crystalline size (*D*), dislocation density ( $\delta$ ), strain ( $\epsilon$ ) and crystalline phase from the analysis of XRD spectra in Fig. 1.

crystalline phase for various milling time of CuO/ZnO composite. 1 h milling time shows higher crystalline phase due to the lattice match between Cu and Zn being high, and it decreases to become the dominant amorphous phase after 12 h. This argument is consistent with dislocation density which correlated with the number of defects present in the composite CuO/ZnO. For increasing the milling time, the number of defects may due to the breaking bond also increasing, which is responsible for decreasing the crystalline phase. Crystallite size shows decreasing with increasing the milling time due to the atoms of Zn and Cu spread each other that produce the individual crystal structure [47]. The strain increases with increasing the milling time due to the non-uniform of the lattice structure [48]. The milling time of 44–52 h shows decreasing sharply of the strain due to the atoms of the Zn replaced some of the oxygen atoms in the lattice of CuO structure or vice versa, which affects in increasing the uniform structure [49]. This effect can be seen clearly in the diffraction peaks which were shifted to the higher 2 $\theta$  positions.

### 3.2. FTIR spectroscopy

Fig. 3 shows the FTIR of CuO/ZnO composite recorded in the range of 350–1,200  $\text{cm}^{-1}$ . The vibration band wavelength strongly depends on the crystallite size, the chemical composition, and the morphology of composites [50]. The band located at 400 to 590  $\text{cm}^{-1}$  is probably attributed to the Zn–O stretching mode bonding with Cu in the form Zn–O–Cu [51]. For 40 h of milling time, the absorption peak is higher than other milling times due to the Zn atoms filling the oxygen atoms in the CuO lattice structure or vice versa which affected in increasing the uniform structure, but it could be different lattice parameters [49].

Suryani et al. [41] the quantitative analysis of the FTIR spectra is used to determine the optical properties, the dielectric functions, and the energy-loss functions as a function of the wavenumber by applying the Kramers–Kronig relations. The Kramers–Kronig relation is also usually used in the quantitative analysis of electron spectroscopy spectra to determine the optical and dielectric properties of various

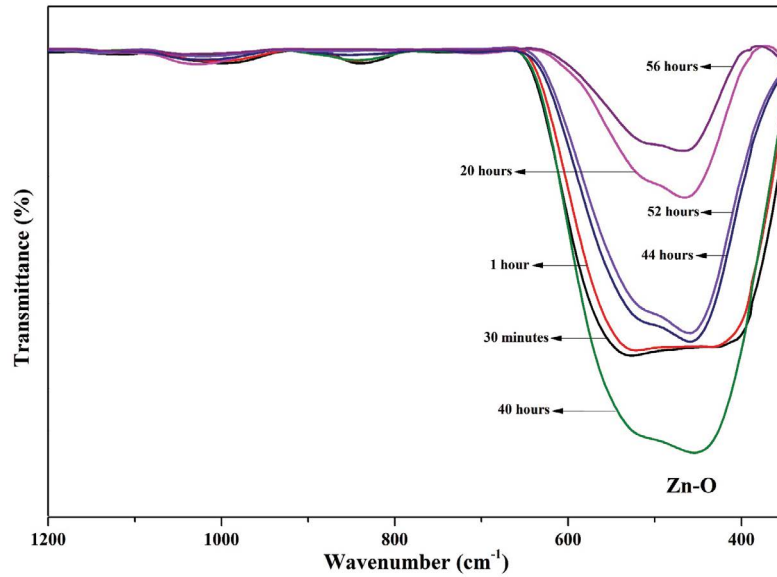


Fig. 3. Fourier-transform infrared (FTIR) spectra of composite CuO/ZnO for several milling times.

materials as reported [52–59]. From the quantitative analysis of FTIR spectra, the optical properties in the form of refractive index  $n(\omega)$  and extinction coefficient  $k(\omega)$ , real and imaginary dielectric function, and the energy-loss function were determined. Khorrami et al. [60] reported the FTIR spectra in the form of a transmittance spectrum needed to convert to the reflectance spectrum by the equation:

$$A(\omega) = 2 - \log[T(\omega)\%] \quad (3)$$

$$R(\omega) = 100 - [T(\omega) + A(\omega)] \quad (4)$$

The reflection spectra are used for determining the  $n(\omega)$  and  $k(\omega)$  as follows [61,62]:

$$n(\omega) = \frac{1 - R(\omega)}{1 + R(\omega) - 2\sqrt{R(\omega)}\cos\phi(\omega)} \quad (5)$$

$$k(\omega) = \frac{2\sqrt{R(\omega)}\sin\phi(\omega)}{1 + R(\omega) - 2\sqrt{R(\omega)}\cos\phi(\omega)} \quad (6)$$

where  $\phi(\omega)$  is the phase change between photon from FTIR spectroscopy with reflections after traveling inside the sample which can be written:

$$\phi(\omega) = -\frac{4\omega}{\pi} \int_0^\infty \frac{\ln R(\omega') - \ln R(\omega)}{\omega'^2 - \omega^2} \quad (7)$$

By applying Kramers–Kronig relation, Eq. (7) becomes:

$$\phi(\omega_j) = -\frac{4\omega_j}{\pi} x\Delta\omega x \sum_i \frac{\ln(\sqrt{R(\omega)})}{\omega_i^2 - \omega_j^2} \quad (8)$$

where  $j$  is a series of wavenumber, if  $j$  is an odd number so then  $i$  parts is 2, 4, 6, 8, ...,  $j-1$ ,  $j+1$ . While wavenumber  $j$  is an even,  $i$  parts is 1, 3, 5, 7, ...,  $j-1$ ,  $j+1$ , ...,  $\Delta\omega = \omega_{j+1} - \omega_j$ . The optical properties are presented in Fig. 4 for several various milling times (30 min, 1, 20, 40, 44, 52, and 56 h). The cross-point between  $n$  and  $k$  is related to the optical intersection at the lattice indicated by TO for transverse optical phonon vibration mode at lower wavelength and longitudinal optical (LO) for longitudinal optical phonon vibration mode at higher wavelength as can be seen in Fig. 4 (first rows) and the corresponding result presented in Table 2.

The real part  $\epsilon_1(\omega)$  and the imaginary part  $\epsilon_2(\omega)$  of the dielectric function is  $n$  determined from the relations as follows:

$$\epsilon_1(\omega) = n^2(\omega) - k^2(\omega) \quad (9)$$

$$\epsilon_2(\omega) = 2n(\omega)k(\omega) \quad (10)$$

Fig. 3 (second rows) shows real ( $\epsilon_1(\omega)$ ) and imaginary parts ( $\epsilon_2(\omega)$ ) of the dielectric function at the middle rows for CuO/ZnO composites for various milling times, respectively. The main peak position of imaginary parts ( $\epsilon_2(\omega)$ ) of the dielectric function in the wavelength ranges from 400 to 460  $\text{cm}^{-1}$  also is used to determining TO optical vibration mode.

Ghasemifard et al. [63] and Legan et al. [64] reported that the LO vibration modes can be identified by two ways; first, from the cross-point between  $n(\omega)$  and  $k(\omega)$  (first row in Fig. 3) and second, from the energy-loss function ( $\text{Im}(-1/e(\omega)) = (\epsilon_1(\omega))/(\epsilon_1^2(\omega) + \epsilon_2^2(\omega))$ ) [38] (third rows in Fig. 4). As shown in Table 2, the LO decreases from 927  $\text{cm}^{-1}$  for milling time 30 min to 626  $\text{cm}^{-1}$  for 20 h indicated that the phase changed from crystalline to amorphous phase which consistent with analysis of XRD spectra. For 40 h, the LO is higher which indicates the dominant amorphous

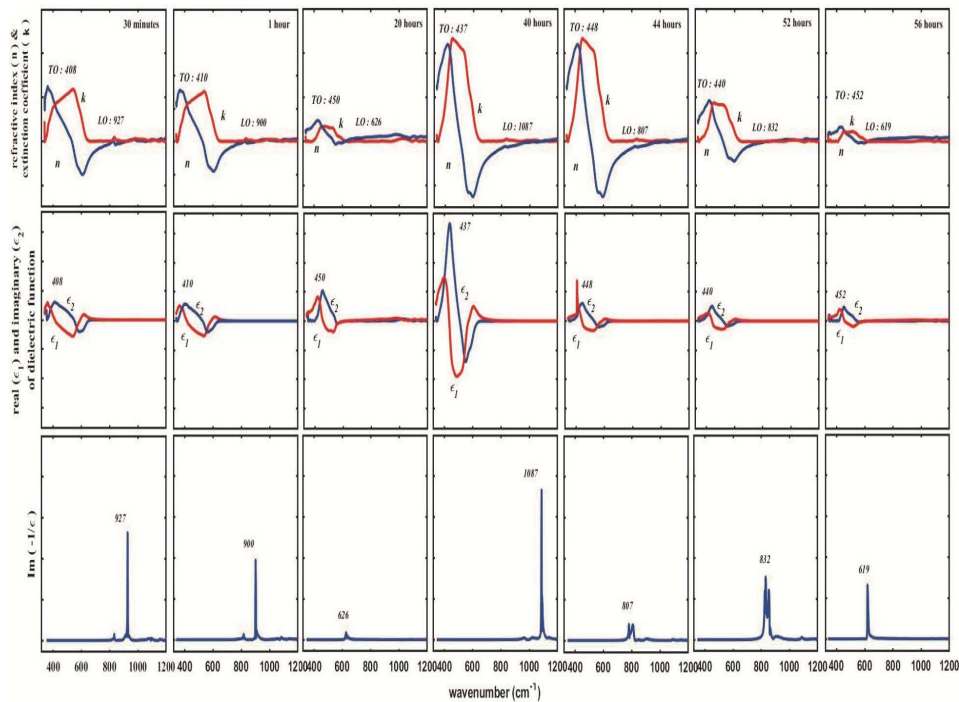


Fig. 4. Quantitative analysis of FTIR spectra in Fig. 3 for determining the optical properties ( $n$  and  $k$ ) (first rows), the real  $\epsilon_1(\omega)$  and the imaginary  $\epsilon_2(\omega)$  part of the dielectric function (second rows), and the energy-loss function  $\text{Im}(-1/\epsilon)$  (third rows) of composite CuO/ZnO for various milling times. The longitudinal and transversal optical phonon modes are indicated by LO and TO, respectively.

Table 2

Frequencies of optical phonon mode (LO) for longitudinal and (TO) for transversal, the main peaks of the real part  $\epsilon_1(\omega)$  and imaginary part  $\epsilon_2(\omega)$  of the dielectric function and the distance of optical phonon

| Milling time (h) | $\epsilon_1(\omega)$ (cm <sup>-1</sup> ) | $\epsilon_2(\omega)$ (cm <sup>-1</sup> ) | LO (cm <sup>-1</sup> ) | TO (cm <sup>-1</sup> ) | $\Delta$ (LO – TO) (cm <sup>-1</sup> ) | $\text{Im}(-1/\epsilon)$ (cm <sup>-1</sup> ) | FWHM $\text{Im}(-1/\epsilon)$ (cm <sup>-1</sup> ) |
|------------------|--|--|------------------------|------------------------|--|--|---|
| 0.5              | 363                                      | 408                                      | 927                    | 408                    | 519                                    | 927  | 22  |
| 1                | 364                                      | 410                                      | 900                    | 410                    | 490                                    | 900  | 11  |
| 20               | 424                                      | 450                                      | 626                    | 450                    | 176                                    | 626  | 10  |
| 40               | 418                                      | 437                                      | 1,087                  | 437                    | 650                                    | 1,087  | 11  |
| 44               | 417                                      | 448                                      | 807                    | 448                    | 359                                    | 807  | 28  |
| 52               | 420                                      | 440                                      | 832                    | 440                    | 392                                    | 832  | 38  |
| 56               | 434                                      | 452                                      | 619                    | 452                    | 167                                    | 619  | 4   |

phase. The consistency and validation of the method in this study in analysing FTIR spectra by using Kramers–Kronig relation are continuous for various type of materials: composites cement/BaSO<sub>4</sub>/Fe<sub>3</sub>O<sub>4</sub> [40], composite geopolymers fly ash-metal [65], Co/Fe<sub>2</sub>O<sub>3</sub> composites by additional activated carbon [66], zinc hydroxide nanoparticle [67], composites Fe/CNs/PVA [68], bioplastics (SPF/starch/chitosan/polypropylene) [69], and composite carbon-lignin/zinc oxide nanocrystalline [2]. This method also successfully is used to identify the plasma frequency from the main peak position of the energy-loss function ( $\text{Im}(-1/e(\omega))$ ).

The real part  $\epsilon_1(\omega)$  and the imaginary part  $\epsilon_2(\omega)$  of the dielectric function is used as input parameter for determining the optical absorption coefficient as follows:

$$\alpha(\omega) = \sqrt{2}\omega \left[ \sqrt{\epsilon_1(\omega)^2 + \epsilon_2(\omega)^2} - \epsilon_1(\omega) \right]^{\frac{1}{2}} \quad (11)$$

The calculation results of the optical absorption coefficient are presented in Fig. 5. The absorption peak in the wavelength between 400 to 600 nm indicated the region of Far-IR. The optical absorption contributed from the position of Cu, O, and Zn atom in composite CuO/ZnO consequently to the lattice vibration. For 30 min and 1 h milling, it shows peak of the absorption coefficient about  $4 \times 10^5$  cm<sup>-1</sup> and decrease to about  $0.5 \times 10^5$  cm<sup>-1</sup> for 20 h milling times. For 44 and 56 h, it shows a low optical absorption coefficient for 20 h but for 40 and 52 h, it shows high optical

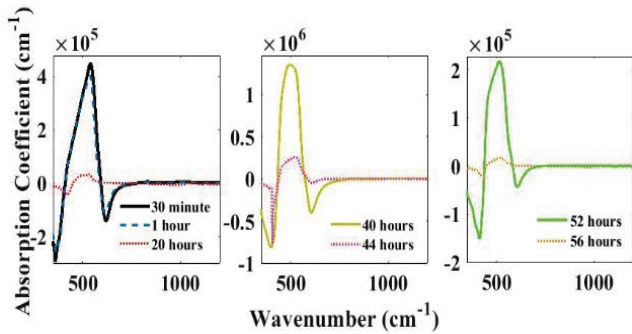


Fig. 5. Optical absorption coefficient determined from the real  $\epsilon_1(\omega)$  and imaginary  $\epsilon_2(\omega)$  parts of the dielectric function in the second rows of Fig. 4.

absorption similar to 1 h. These phenomena may be due to the lattice condition which can be shortening or enlarging, and it shows consistent with the distance ( $\Delta$ ) between two optical phonon vibration mode [41,61–64].

Fig. 6 and Table 2 show the relation between the real part  $\epsilon_1(\omega)$  of the dielectric function, the distance ( $\Delta$ ) between LO and TO, the FWHM of  $\text{Im}(-1/\epsilon)$ , and the TO optical phonon mode for milling time (30 min, 1, 20, 40, 44, 52 and 56 h). By this method, there are two relations: first, the relation between the real part  $\epsilon_1(\omega)$  of the electric function and TO. The second, relation between the FWHM  $\text{Im}(-1/\epsilon)$  and the  $\epsilon_1(\omega)$ . For 44–52 h, the FWHM of  $\text{Im}(-1/\epsilon)$  is higher due to the broken bond between Cu–O and Zn–O which are higher in the composite, which is consistent with the strain ( $\epsilon$ ) in Table 1. For 20 h of milling times, it shows the distance ( $\Delta$ ) between two optical phonon modes

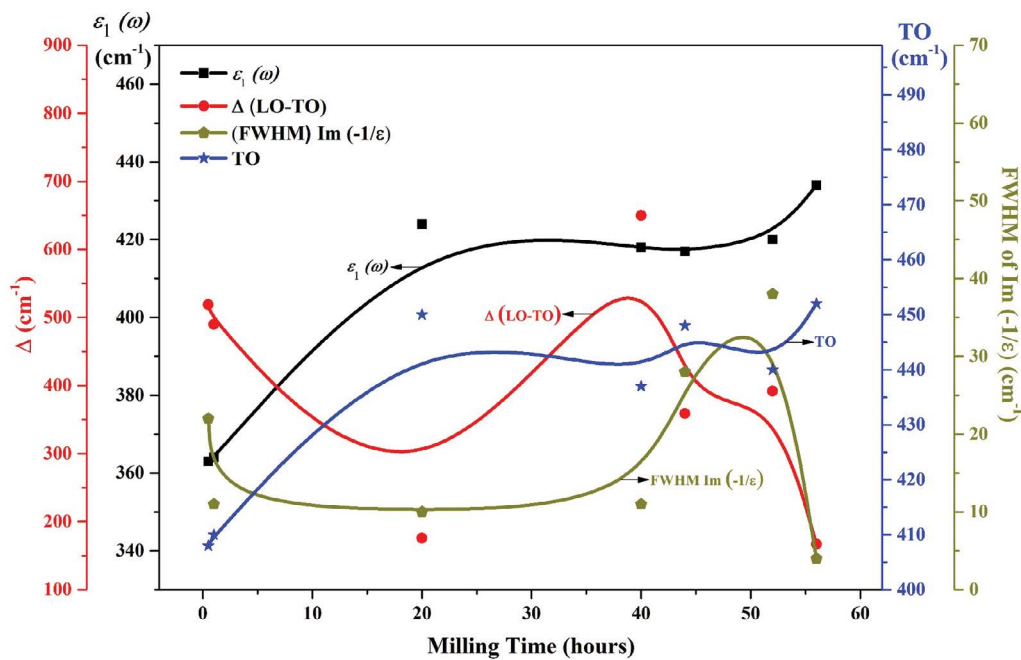


Fig. 6. Relation between the real part  $\epsilon_1(\omega)$  of the electric function, splitting ( $\Delta$ ) between LO and TO, and FWHM of energy-loss function  $\text{Im}(-1/\epsilon)$ .

that is minimum due to the enlarging of the lattice caused by the atoms of Cu sitting in the middle of ZnO lattice [70] which consistent with the crystallite size increasing as can be seen in Table 1.

### 3.3. Density of states

The density of states (DOS) calculation is determined by using the first-principles pseudopotential which is based on the density functional theory (DFT) and the plane wave method. It is implemented in the quantum espresso which stands for open source package for research electronic structure, simulation, and optimization. The effects of exchange and correlation are carried out with Perdew Burke-Ehrenk of (PBE) functional under treated the generalized-gradient-approximation. The ultrasoft pseudopotential (USP) method is used to analysis the interaction of electrons [71].

As shown in Fig. 7, the graph DOS was observed from peak  $-8$  to  $17$  eV. It can be observed the peak from  $-7.5$  to  $0$  eV that corresponds to the occupied valance band, and the group from  $2.5$  to  $15$  eV corresponds to the occupied conduction band. The result of DOS is rather similar of  $\text{CuZnO}_2$ . The value of DOS is rather similar for each composite due to the crystalline phase (%) for composites that are similar as shown in Table 1 [72].

### 3.4. UV-Vis spectrophotometer

The UV-Vis spectra were measured and recorded to analysis the optical band gap in the composite  $\text{CuO}/\text{ZnO}$  as a function of milling time. Based on another report, the optical band gap of ZnO is estimated to be  $\sim 3.25$  eV. For comparison, CuO nanoparticle has the photon energy of  $\sim 1.5$  eV.

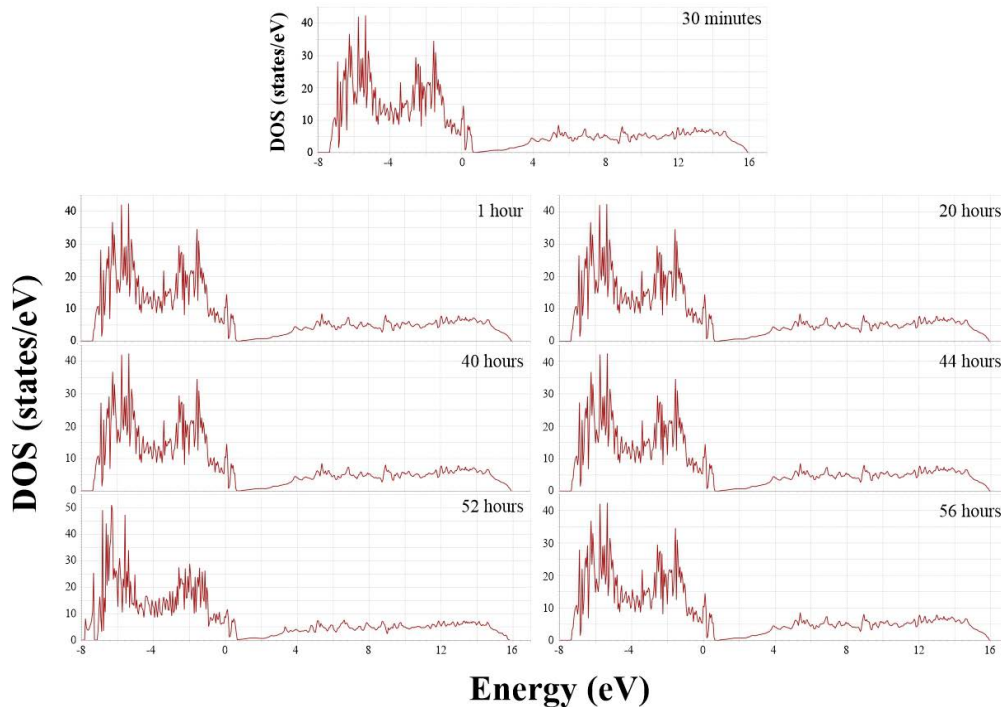


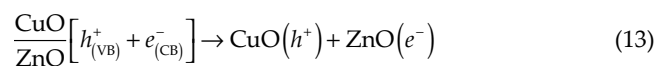
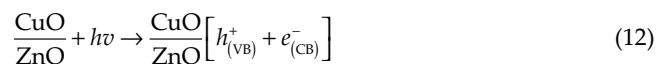
Fig. 7. Density of states (DOS) of composite CuO/ZnO for several milling time.

Fig. 8 shows the band gap energies obtained by the Tauc's plot methods. The value of the band gap energy of composites was shown to be about  $\sim 3$  eV. The result of the band gap indicated that the CuO and ZnO were successfully synthesized by using solid state method. The band gap value of composite CuO/ZnO as a function of milling time shows a good agreement with the result of the previous experiment [73].

Fig. 9a and b show the absorption of UV-Vis spectra for 15 min and 30 min irradiation time for various milling time (30 min, 1, 20, 40, 44, 52, and 56 h) for determining photocatalytic performance using methylene blue (MB) as a pollutant model. The percentage of degradation as can be seen in Fig. 9c calculated by using the equation;  $D(\%) = \frac{C_0 - C_t}{C_0} \times 100$ , where  $C_0$  is the control absorbance before irradiation, and  $C_t$  is the absorbance after irradiation time [74–76]. The best degradation percentage is for 1 h of milling time, which reaching 96.8% for 30 min irradiation due to the time higher crystalline phase. Is along with 20 h up to 52 h milling time the degradation decreased, but for 56 h, the degradation increases again that the trend is opposite with the FWHM of  $\text{Im}(-1/\epsilon)$  in Table 2. Fig. 9d shows the degradation rate as a function of milling time. The photocatalyst performance is observed from the rate constant of degradation ( $k_r$ ), where the high value of  $k_r$  indicated good performance indicated by the highest intensity in Fig. 7d. The  $k_r$  is determined from the first-order plot using the following equation  $-\ln(C_t/C_0) = k_r t$ , where  $C_0$  is the initial absorbance, and  $C_t$  is the absorbance at a time. It shows highest intensity indicated the highest  $k_r$  [77].

Fig. 9e shows that there was no noticeable reduction in photodegradation efficiency even after recycling. It was

observed that the reduction rate of photocatalytic after the second cycle of less than 0.6% indicates the stability of the composite. Fig. 9f shows the photocatalytic mechanism for composite CuO/ZnO. The electronic structures of semiconductor materials show two-level bands. The highest band with filled by the electron is referred to as the valence band (VB) and the lowest unoccupied band referred to as the conduction band (CB). Irradiation of composite CuO/ZnO produces electron ( $e^-$ ) jump to the CB and remaining hole ( $h^+$ ) at the valence band in an aqueous solution dissolved oxygen and oxidable pollutant [78]. The complete degradation mechanism of MB can be understood by the following chemical reaction of CuO/ZnO:



#### 4. Conclusions

In this work, composite CuO/ZnO successfully is synthesized using mechanical alloying to find the phase transformation, the structural properties including;  $d$ -spacing,

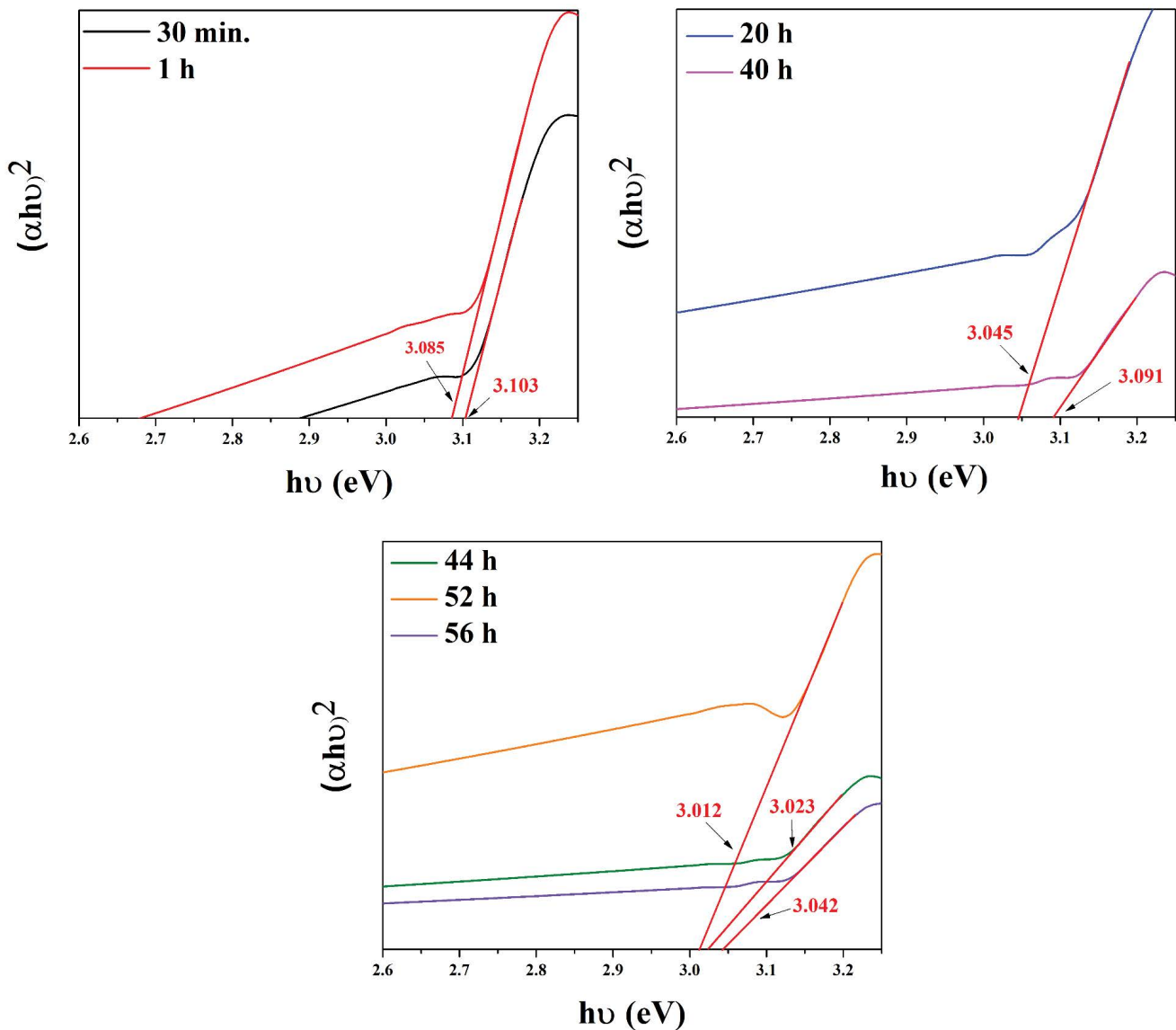


Fig. 8. Band gap analyses of composite CuO/ZnO for several milling time.

the crystallite size ( $D$ ), dislocation density ( $\delta$ ), strain ( $\epsilon$ ), and crystalline phase from the quantitative analysis of X-ray diffraction. The reflective index ( $n$ ), extinction coefficient ( $k$ ), real part ( $\epsilon_1$ ) and imaginary part ( $\epsilon_2$ ) of the dielectric function, energy-loss function ( $\text{Im}(-1/\epsilon_1(\omega))$ ) is studied from the quantitative analysis of FTIR spectra by applying Kramers–Kronig relation. The crystallite size decreases with increasing the milling time due to the Zn and Cu atoms spreading each other and producing the individual crystal structure. The strain for 44–52 h decreases sharply due to the atoms of the Zn replacing some of the oxygen atoms in the lattice of CuO structure or vice versa which affected in increasing the structure uniformly. The FWHM of  $\text{Im}(-1/\epsilon)$  for 44–52 h is higher due to the broken bond between Cu–O and Zn–O is higher in the composite confirmed by the strain ( $\epsilon$ ) value. The distance ( $\Delta$ ) between two optical phonon modes for 20 h of milling times shows

minimum due to the lattice enlarging caused by the atoms of Cu sitting in the middle of ZnO lattice. This study shows that the XRD spectra is effective way to investigate the phase transformation, structural properties, and FTIR spectra is powerful way to determine optical properties of composite CuO/ZnO. The density of states was calculated by using quantum espresso package. The value of DOS is rather similar for each composite due to the crystalline phase (%) for composites that are similar. The best degradation is 1 h milling, which reached 96.8% for 30 min irradiation time.

#### Acknowledgement

This work was supported by the PDPA (Penelitian Dosen PA) 2020 grant: 1585/UN4.22/PT.01.03/2020 funded by the Hasanuddin University (UNHAS).

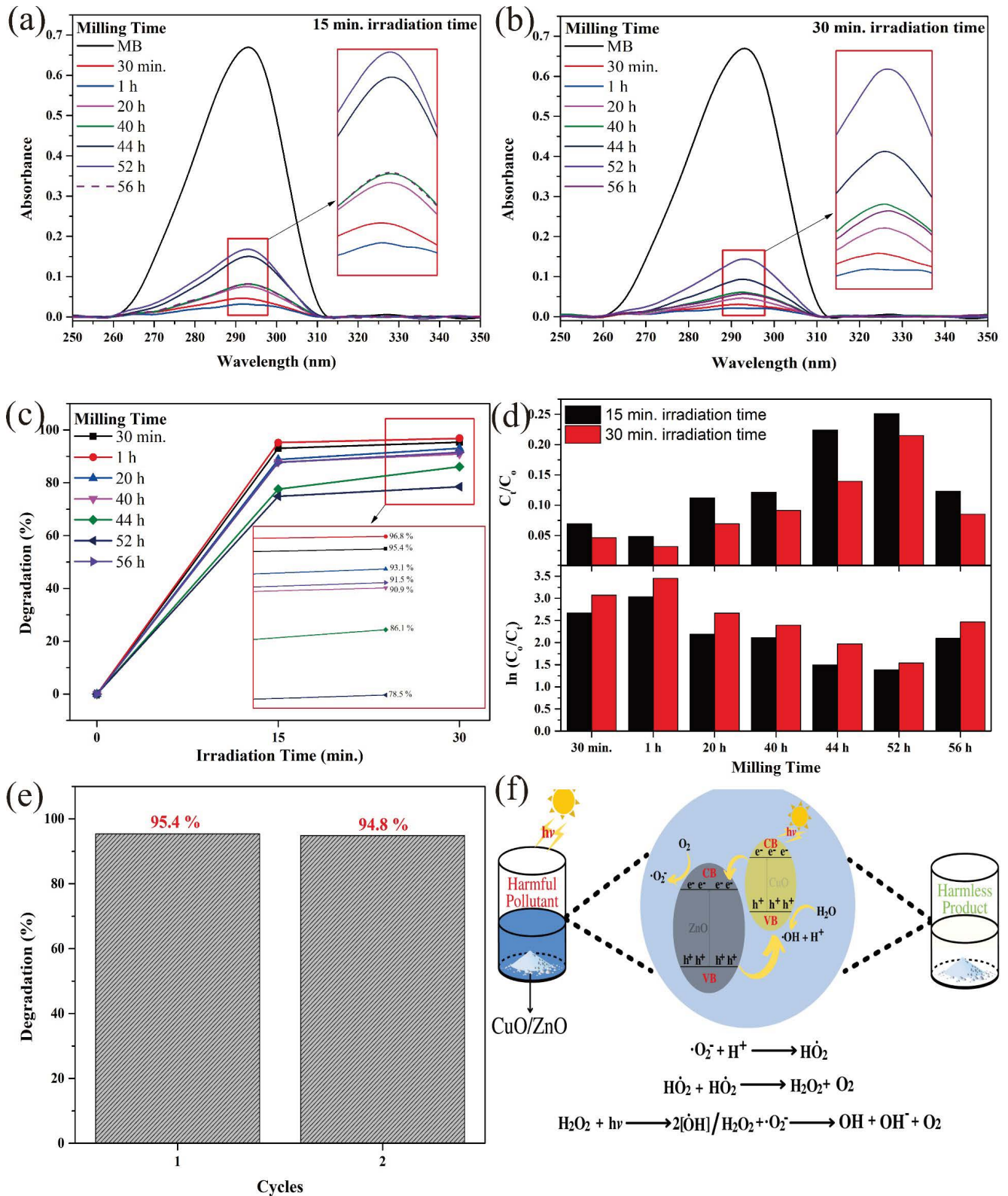


Fig. 9. (a) UV-Vis absorption spectra (15 min irradiation time), (b) UV-Vis absorption spectra (30 min irradiation time), (c) percentage of degradation, (d) photocatalytic performance and kinetic curve of photocatalytic, (e) cycles of degradation efficiency, and (f) photodegradation mechanism for MB in the presence of CuO/ZnO as a function of milling time.

## References

- [1] S. Ilyas, B. Abdullah, D. Tahir, Enhancement of absorbing frequency and photo-catalytic performance by temperature treatment of composites Fe<sub>3</sub>O<sub>4</sub>-AC nanoparticle, *Adv. Powder Technol.*, 31 (2020) 905–913.
- [2] B. Ulum, S. Ilyas, A.N. Fahri, I. Mutmainna, M.A. Anugrah, N. Yudasari, E.B. Demmalino, D. Tahir, Composite carbon-lignin/zinc oxide nanocrystalline ball-like hexagonal mediated from *Jatropha curcas* L leaf as photocatalyst for industrial dye degradation, *J. Inorg. Organomet. Polym.*, 30 (2020) 4905–4916.
- [3] H. Wang, X. Li, X. Zhao, C. Li, X. Song, P. Zhang, P. Huo, X. Li, A review on heterogeneous photocatalysis for environmental remediation: from semiconductors to modification strategies, *Chin. J. Catal.*, 43 (2022) 178–214.
- [4] R.K. Nekouei, F. Pahlevani, R. Rajarao, R. Golmohammadzadeh, V. Sahajwalla, Direct transformation of waste printed circuit boards to nano-structured powders through mechanical alloying, *Mater. Des.*, 141 (2018) 26–36.
- [5] N. Loudjani, T. Gouasmia, M. Bououdina, J.L. Bobet, Phase formation and magnetic properties of nanocrystalline Ni<sub>70</sub>Co<sub>30</sub> alloy prepared by mechanical alloying, *J. Alloys Compd.*, 846 (2020) 156392, doi: 10.1016/j.jallcom.2020.156392.
- [6] A. Ghasedi, E. Koushki, M. Zirak, H. Alehdaghi, Improvement in structural, electrical, and optical properties of Al-doped ZnO nanolayers by sodium carbonate prepared via sol-gel method, *Appl. Phys. A*, 126 (2020) 474, doi: 10.1007/s00339-020-03663-7.
- [7] B. Arik, Characterization and wrinkle resistance enhancement by sol-gel method of variously pretreated linen fabrics, *Fibers Polym.*, 21 (2020) 82–89.
- [8] P.C. Torres-Mayanga, D. Lachos-Perez, A. Mudhoo, S. Kumar, A.B. Brown, M. Tyufekchiev, G. Dragone, S.I. Mussatto, M.A. Rostagno, M. Timko, T. Forster-Carneiro, Production of biofuel precursors and value-added chemicals from hydrolysates resulting from hydrothermal processing of biomass: a review, *Biomass Bioenergy*, 130 (2019) 105397, doi: 10.1016/j.biombioe.2019.105397.
- [9] K. Suwa, L. Cojocaru, K. Wienands, C. Hofmann, P.S.C. Schulze, A.J. Bett, K. Winkler, J.C. Goldschmidt, S.W. Glunz, H. Nishide, Vapor-phase formation of a hole-transporting thiophene polymer layer for evaporated perovskite solar cells, *ACS Appl. Mater. Interfaces*, 12 (2020) 6496–6502.
- [10] M.A. Davenport, M.P. Confer, T.C. Douglas, T.B. Rawot Chhetri, J.M. Allred, Large single crystals of V<sub>1-x</sub>Mo<sub>x</sub>O<sub>2</sub> from a two-step chemical vapor transport synthesis, *Cryst. Growth Des.*, 20 (2020) 3635–3640.
- [11] N. Liao, D. Jia, Z. Yang, Y. Li, Improved toughness of ZrB<sub>2</sub>-SiC composites with nanopowders obtained by mechanical alloying, *J. Phys. Chem. Solids*, 136 (2020) 109153, doi: 10.1016/j.jpcs.2019.109153.
- [12] B.D. Long, N.V. Khanh, D.N. Binh, N.H. Hai, Thermoelectric properties of quaternary chalcogenide Cu<sub>2</sub>ZnSnS<sub>3</sub>, synthesized by mechanical alloying, *Powder Metall.*, 63 (2020) 220–226.
- [13] A.A.A. Joubori, C. Suryanarayana, Synthesis of stable and metastable phases in the Ni-Si system by mechanical alloying, *Powder Technol.*, 302 (2016) 8–14.
- [14] W. Zhang, P. Li, X. Zou, Z. Yu, X. Yang, X. Pan, Y. Zhao, Y. Zhang, Equiaxial nano-crystals Nb<sub>3</sub>Al superconductor prepared by optimized mechanically alloying, *J. Mater. Sci.*, 54 (2019) 5022–5031.
- [15] J.-K. Han, K.-D. Liss, T.G. Langdon, M. Kawasaki, Synthesis of a bulk nanostructured metastable Al alloy with extreme supersaturation of Mg, *Sci. Rep.*, 9 (2019) 17186, doi: 10.1038/s41598-019-53614-3.
- [16] Y. Xu, Y. Sin, X. Dai, B. Liao, S. Zhou, D. Chen, Microstructure and magnetic properties of amorphous/nanocrystalline Ti<sub>30</sub>Fe<sub>70</sub> alloys prepared by mechanical alloying, *J. Mater. Res. Technol.*, 8 (2019) 2486–2493.
- [17] R. Titorenkova, E. Dyulgerova, V. Petkova, R. Ilieva, Carbonation and dihydroxylation of apatite during high energy milling of biphasic Ca-phosphate ceramics, *Ceram. Int.*, 45 (2019) 7025–7033.
- [18] M. Mursalat, M. Schoenitz, E.L. Dreizin, Composite Al-Ti powders prepared by high-energy milling with different process controls agents, *Adv. Powder Technol.*, 30 (2019) 1319–1328.
- [19] V.M. Tabie, X. Shi, J. Li, C. Cai, X. Xu, Tribological properties of Ti-4Si-xZr-yY<sub>2</sub>O<sub>3</sub>/5TiO<sub>2</sub> composites prepared by high-energy milling, cold pressing and sintering, *Int. J. Precis. Eng. Manuf.*, 20 (2019) 1929–1937.
- [20] S. Ambika, M. Devasena, I.M. Nambi, Synthesis, characterization, and performance of high energy ball milled meso-scale zero valent iron in Fenton reaction, *J. Environ. Manage.*, 181 (2016) 847–855.
- [21] X. Ma, J. Wen, S. Zhang, H. Yuan, K. Li, F. Yan, X. Zhang, Y. Chen, Crystal Co<sub>3</sub>B (x = 1–3) synthesized by a ball-milling method as high-performance electrocatalysts for the oxygen evolution reaction, *ACS Sustainable Chem. Eng.*, 5 (2017) 10266–10274.
- [22] L.S. de Oliveira, M. de Oliveira Melquiades, C. da Costa Pinto, D.M. Trichês, S.M. de Souza, Phase transformations in a NiTiGe system induced by high energy milling, *J. Solid State Chem.*, 281 (2020) 121056, doi: 10.1016/j.jssc.2019.121056.
- [23] A.T. Ochoa, N. Kametani, C.C. Gallardo, J.E.L. Sillas, N. Adachi, Y. Todaka, J.M.H. Ramirez, Formation of a metastable FCC phase and high Mg solubility in the Ti-Mg system by mechanical alloying, *Powder Technol.*, 374 (2020) 348–352.
- [24] C.-L. Chen, Suprianto, Microstructure and mechanical properties of AlCuNiFeCr high entropy alloy coatings by mechanical alloying, *Surf. Coat. Technol.*, 386 (2020) 125443, doi: 10.1016/j.surfcoat.2020.125443.
- [25] S. Ghobrial, D.W. Kirk, S.J. Thorpe, Solid state amorphization in the Ni-Nb-Y system by mechanical alloying, *J. Non-Cryst. Solids*, 502 (2018) 1–8.
- [26] S.N. Alam, N. Sharma, D. Panda, A. Kumar, D. Sampenga, A. Sairam, V. Sarky, M.B. Krupateja, Mechanical milling of Al and synthesis of in-situ Al<sub>2</sub>O<sub>3</sub> particles by mechanical alloying of Al-CuO system, *J. Alloys Compd.*, 735 (2018) 799–812.
- [27] R. Ratnawulan, R. Ramli, A. Fauzi, S.H. AE, Synthesis and characterization of polystyrene/CuO-Fe<sub>2</sub>O<sub>3</sub> nanocomposites from natural materials as hydrophobic photocatalytic coatings, *Crystals*, 11 (2021) 31, doi: 10.3390/cryst11010031.
- [28] P.V. Viet, T.H. The Vinh, N.T.N. Dung, C.M. Thi, Facile ball-milling synthesis of TiO<sub>2</sub> modified ZnO for efficient photocatalytic removal of atmospheric nitric oxide gas under solar light irradiation, *Chem. Phys. Lett.*, 775 (2021) 138642, doi: 10.1016/j.cplett.2021.138642.
- [29] J. Singh, S. Sharma, S. Soni, S. Sharma, R.C. Singh, Influence of different milling media on structural, morphological and optical properties of the ZnO nanoparticles synthesized by ball milling process, *Mater. Sci. Semicond. Process.*, 98 (2019) 29–38.
- [30] A. Saboor, S.M. Shah, H. Hussain, Band gap tuning and applications of ZnO nanorods in hybrid solar cell: Ag-doped versus Nd-doped ZnO nanorods, *Mater. Sci. Semicond. Process.*, 93 (2019) 215–225.
- [31] P. Wang, Y. Wang, L. Ye, M. Wu, R. Xie, X. Wang, X. Chen, Z. Fan, J. Wang, W. Hu, Ferroelectric localized field-enhanced ZnO nanosheet ultraviolet photodetector with high sensitivity and low dark current, *Small*, 14 (2018) 1800492, doi: 10.1002/sml.201800492.
- [32] N. Akhtar, S.K. Metkar, A. Girigoswami, K. Girigoswami, ZnO nanoflower based sensitive nano-biosensor for amyloid detection, *Mater. Sci. Eng., C*, 78 (2017) 960–968.
- [33] Y.H. Navale, S.T. Navale, F.J. Stadler, N.S. Ramgir, V.B. Patil, Enhanced NO<sub>2</sub> sensing aptness of ZnO nanowire/CuO nanoparticle heterostructure-based gas sensors, *Ceram. Int.*, 45 (2019) 1513–1522.
- [34] R. Ahmad, M.S. Ahn, Y.B. Hahn, Fabrication of a non-enzymatic glucose sensor field-effect transistor based on vertically-oriented ZnO nanorods modified with Fe<sub>2</sub>O<sub>3</sub>, *Electrochem. Commun.*, 77 (2017) 107–111.
- [35] S.K. Kokate, C.V. Jagtap, P.K. Baviskar, S.R. Jadhav, H.M. Pathan, K.C. Mohite, CdS sensitized cadmium doped ZnO solar cell: fabrication and characterizations, *Optik*, 157 (2018) 628–643.
- [36] F.X. Liang, Y. Gao, C. Xie, X.W. Tong, Z.J. Li, L.B. Luo, Recent advances in the fabrication of graphene-ZnO heterojunctions

- for optoelectronic device applications, *J. Mater. Chem. C*, 6 (2018) 3815–3833.
- [37] W. Li, Y. Li, D. Zhang, Y. Lan, J. Guo, CuO-Co<sub>3</sub>O<sub>4</sub>@CeO<sub>2</sub> as a heterogeneous catalyst for efficient degradation of 2,4-dichlorophenoxyacetic acid by peroxydisulfate, *J. Hazard. Mater.*, 381 (2020) 121209, doi: 10.1016/j.jhazmat.2019.121209.
- [38] X. Zhang, G. Zhang, S. Wang, S. Li, S. Jiao, Porous CuO microspheres architectures as high-performance cathode materials for aluminum-ion battery, *J. Mater. Chem. A*, 6 (2018) 3084–3090.
- [39] M. Poloju, N. Jayababu, M.V. Ramana Reddy, Improved gas sensing performance of Al doped ZnO/CuO nanocomposite based ammonia gas sensor, *Mater. Sci. Eng., B*, 227 (2018) 61–67.
- [40] A. Khataee, D. Kalderis, P. Gholami, A. Fazli, M. Moschogiannaki, V. Binas, M. Lykaki, M. Konsolakis, Cu<sub>2</sub>O-CuO@biochar composite: synthesis, characterization and its efficient photocatalytic performance, *Appl. Surf. Sci.*, 498 (2019) 143846, doi: 10.1016/j.apsusc.2019.143846.
- [41] S. Suryani, H. Heryanto, R. Rusdaeni, A.N. Fahri, D. Tahir, Quantitative analysis of diffraction and infra-red spectra of composite cement/BaSO<sub>4</sub>/Fe<sub>3</sub>O<sub>4</sub> for determining correlation between attenuation coefficient, structural and optical properties, *Ceram. Int.*, 46 (2020) 18601–18607.
- [42] Saepurahman, R. Hashaikheh, Insight into ball milling for size reduction and nanoparticles production of H-Y zeolite, *Mater. Chem. Phys.*, 220 (2018) 322–330.
- [43] I. Feijoo, M. Cabeza, P. Merino, G. Pena, M.C. Perez, S. Cruz, P. Rey, Estimation of crystallite size and lattice strain in nano-sized TiC particle-reinforced 6005A aluminium alloy from X-ray diffraction line broadening, *Powder Technol.*, 343 (2019) 19–28.
- [44] A.H. Taghvaei, M. Stoica, G. Vaughan, M. Ghaffari, S. Maleksaeedi, K. Janghorban, Microstructural characterization and amorphous phase formation in Co<sub>40</sub>Fe<sub>22</sub>Ta<sub>3</sub>B<sub>30</sub> powders produced by mechanical alloying, *J. Alloys Compd.*, 512 (2012) 85–93.
- [45] S. Ilyas, Heryanto, B. Abdullah, D. Tahir, X-ray diffraction analysis of nanocomposite Fe<sub>3</sub>O<sub>4</sub>/activated carbon by Williamson–Hall and size-strain plot methods, *Nano-Struct. Nano-Objects*, 20 (2019) 100396, doi: 10.1016/j.nano.2019.100396.
- [46] A.K. Zak, W.H.A. Majid, M.E. Abrishami, R. Yousefi, X-ray analysis of ZnO nanoparticles by Williamson–Hall and size-strain plot methods, *Solid State Sci.*, 13 (2011) 251–256.
- [47] E. Sakher, N. Loudjani, M. Benchiheb, M. Bououdina, Influence of milling time on structural and microstructural parameters of Ni<sub>50</sub>Ti<sub>50</sub> prepared by mechanical alloying using Rietveld analysis, *J. Nanomater.*, 2018 (2018) 2560641, doi: 10.1155/2018/2560641.
- [48] P. Singh, A. Abhash, B.N. Yadav, M. Shafeeq, I.B. Singh, D.P. Mondal, Effect of milling time on powder characteristics and mechanical performance of Ti4wt%Al alloy, *Powder Technol.*, 342 (2019) 275–287.
- [49] R. Mayahi, A. Shokuhfar, M.R. Vaezi, Characterization and thermodynamic study of nanostructured Cu-26Zn-4Al (wt.%) shape memory alloy through mechanical alloying, *Mater. Sci. Eng.*, 51 (2020) 153–162.
- [50] B.K. Das, T. Das, K. Parashar, A. Thirumurugan, S.K.S. Parashar, Structural, band gap tuning and electrical properties of Cu doped ZnO nanoparticles synthesized by mechanical alloying, *J. Mater. Sci.: Mater. Electron.*, 28 (2017) 15127–15134.
- [51] A.A.M. Sakib, S.M. Masum, J. Hoinkis, R. Islam, M.A.I. Molla, Synthesis of CuO/ZnO nanocomposites and their application in photodegradation of toxic textile dye, *J. Compos. Sci.*, 3 (2019) 91, doi: 10.3390/jcs3030091.
- [52] D. Tahir, S. Tougaard, Electronic and optical properties of Cu, CuO and Cu<sub>2</sub>O studied by electron spectroscopy, *J. Phys.: Condens. Matter*, 24 (2012) 175002.
- [53] H.C. Shin, D. Tahir, S. Seo, Y.R. Denny, S.K. Oh, H.J. Kang, S. Heo, J.G. Chung, J.C. Lee, S. Tougaard, Reflection electron energy loss spectroscopy for ultrathin gate oxide materials, *Surf. Interface Anal.*, 44 (2012) 623–627.
- [54] D. Tahir, S. Tougaard, Electronic and optical properties of selected polymers studied by reflection electron energy loss spectroscopy, *J. Appl. Phys.*, 111 (2012) 054101, doi: 10.1063/1.3688327.
- [55] D. Tahir, J. Kraer, S. Tougaard, Electronic and optical properties of Fe, Pd, and Ti studied by reflection electron energy loss spectroscopy, *J. Appl. Phys.*, 115 (2014) 243508, doi: 10.1063/1.4885876.
- [56] D. Tahir, S. Ilyas, B. Abdullah, B. Armynah, H.J. Kang, Electronic properties of composite iron (II, III) oxide (Fe<sub>3</sub>O<sub>4</sub>) carbonaceous absorber materials by electron spectroscopy, *J. Electron. Spectrosc. Relat. Phenom.*, 229 (2018) 47–51.
- [57] D. Tahir, S.K. Oh, H.J. Kang, S. Tougaard, Quantitative analysis of reflection electron energy loss spectra to determine electronic and optical properties of Fe–Ni alloy thin films, *J. Electron. Spectrosc. Relat. Phenom.*, 206 (2016) 6–11.
- [58] S. Suryani, Heryanto, D. Tahir, Stopping powers and inelastic mean free path from quantitative analysis of experimental REELS spectra for electrons in Ti, Fe, Ni, and Pd, *Surf. Interface Anal.*, 52 (2019) 1–7.
- [59] Y.R. Denny, H.C. Shin, S. Seo, S.K. Oh, H.J. Kang, D. Tahir, S. Heo, J.G. Chung, J.C. Lee, S. Tougaard, Electronic and optical properties of hafnium indium zinc oxide thin film by XPS and REELS, *J. Electron. Spectrosc. Relat. Phenom.*, 185 (2012) 18–22.
- [60] Gh.H. Khorrami, A. Khorsand Zak, A. Kompany, R. Yousefi, Optical and structural properties of X-doped (X = Mn, Mg, and Zn) PZT nanoparticles by Kramers–Kronig and size strain plot methods, *Ceram. Int.*, 38 (2012) 5683–5690.
- [61] A.K. Zak, W.H.A. Majid, Effect of solvent on structure and optical properties of PZT nanoparticles prepared by sol–gel method, in infrared region, *Ceram. Int.*, 37 (2011) 753–758.
- [62] A. Khorsand Zak, A. Ghanbari, T. Shekofteh-Narm, The effect of molybdenum on optical properties of ZnO nanoparticles in ultraviolet–visible region, *Adv. Powder Technol.*, 28 (2017) 2980–2986.
- [63] M. Ghasemifard, S.M. Hosseini, G.H. Khorrami, Synthesis and structure of PMN–PT ceramic nanopowder free from pyrochlore phase, *Ceram. Int.*, 35 (2009) 2899–2905.
- [64] L. Legan, T. Leskovar, M. Črešnar, F. Cavalli, D. Innocenti, P. Ropret, Non-invasive reflection FTIR characterization of archaeological burnt bones: reference database and case studies, *J. Cult. Heritage*, 41 (2020) 13–26.
- [65] Nurhasmi, Heryanto, A.N. Fahri, S. Ilyas, A. Ansar, B. Abdullah, D. Tahir, Study on optical phonon vibration and gamma ray shielding properties of composite geopolymer fly ash-metal, *Radiat. Phys. Chem.*, 180 (2021) 109250, doi: 10.1016/j.radphyschem.2020.109250.
- [66] D. Tahir, H. Heryanto, S. Ilyas, A.N. Fahri, R. Rahmat, M.H. Rahmi, Y. Taryana, S.G. Sukaryo, Excellent electromagnetic wave absorption of Co/Fe<sub>2</sub>O<sub>3</sub> composites by additional activated carbon for tuning the optical and the magnetic properties, *J. Alloys Compd.*, 864 (2021) 158780, doi: 10.1016/j.jallcom.2021.158780.
- [67] N. Rauf, S. Ilyas, H. Heryanto, R. Rahmat, A.N. Fahri, M.H. Fahri, D. Tahir, The correlation between structural and optical properties of zinc hydroxide nanoparticle in supports photocatalytic performance, *Opt. Mater.*, 112 (2021) 110780, doi: 10.1016/j.optmat.2020.110780.
- [68] Y.K. Lahsmin, H. Heryanto, S. Ilyas, A.N. Fahri, B. Abdullah, D. Tahir, Optical properties determined from infrared spectroscopy and structural properties from diffraction spectroscopy of composites Fe/CNs/PVA for electromagnetic wave absorption, *Opt. Mater.*, 111 (2021) 110639, doi: 10.1016/j.optmat.2020.110639.
- [69] O.S. Jangong, H. Heryanto, R. Rahmat, I. Mutmainna, P.L. Gareso, D. Tahir, Effect of sugar palm fiber (SPF) to the structural and optical properties of bioplastics (SPF/starch/chitosan/polypropylene) in supporting mechanical properties and degradation performance, *J. Polym. Environ.*, 29 (2021) 1694–1705.
- [70] C.-L. Chen, C.-H. Lin, In-situ dispersed La oxides of Al6061 composites by mechanical alloying, *J. Alloys Compd.*, 775 (2019) 1156–1163.
- [71] T. Atsue, I.B. Ogunniranye, O.E. Oyewande, A study of the structural and magnetic properties of nitrides of iron and nickel

- (XN; X = Fe, Ni) using density functional theory approach, *Electron. Struct.*, 2 (2020) 045002.
- [72] V. Nádaždy, K. Gmucová, P. Nádaždy, P. Siffalovic, K. Vegso, M. Jergel, F. Schauer, E. Majkova, Thickness effect on structural defect-related density of states and crystallinity in P3HT thin films on ITO substrates, *J. Phys. Chem. C*, 122 (2018) 5881–5887.
- [73] M.C. Oliveira, V.S. Fonseca, N.F.A. Neto, R.A.P. Ribeiro, E. Longo, S.R. de Lazaro, M.R.D. Bomio, Connecting theory with experiment to understand the photocatalytic activity of CuO–ZnO heterostructure, *Ceram. Int.*, 46 (2020) 9446–9454.
- [74] S. Ilyas, H. Heryanto, D. Tahir, Correlation between structural and optical properties of CuO/carbon nanoparticle in supports the photocatalytic performance and attenuate the electromagnetic wave, *J. Environ. Chem. Eng.*, 9 (2021) 104670, doi: 10.1016/j.jece.2020.104670.
- [75] F.A. AlAbduljabbar, S. Haider, F.A.A. Ali, A.A. Alghyamah, W.A. Almasry, R. Patel, I.M. Mujtaba, TiO<sub>2</sub> nanostructured coated functionally modified and composite electrospun chitosan nanofibers membrane for efficient photocatalytic degradation of organic pollutant in wastewater, *J. Mater. Res. Technol.*, 15 (2021) 5197–5212.
- [76] F.A. AlAbduljabbar, S. Haider, F. Abdulraqeb Ahmed Ali, A.A. Alghyamah, W.A. Almasry, R. Patel, I.M. Mujtaba, Efficient photocatalytic degradation of organic pollutant in wastewater by electrospun functionally modified polyacrylonitrile nanofibers membrane anchoring TiO<sub>2</sub> nanostructured, *Membranes*, 11 (2021) 785, doi: 10.3390/membranes11100785.
- [77] I. Neelakanta Reddy, Ch. Venkata Reddy, M. Sreedhar, J. Shim, M. Cho, D. Kim, Effect of ball milling on optical properties and visible photocatalytic activity of Fe doped ZnO nanoparticles, *Mater. Sci. Eng., B*, 240 (2019) 33–40.
- [78] A. Fouda, S.S. Salem, A.R. Wassel, M.F. Hamza, Th.I. Shaheen, Optimization of green biosynthesized visible light active CuO/ZnO nano-photocatalysts for the degradation of organic methylene blue dye, *Heliyon*, 6 (2020) e04896, doi: 10.1016/j.heliyon.2020.e04896.